Geodesic Tubes for Uncertainty Quantification in Diffusion MRI

Rick Sengers[(✉)], Luc Florack, and Andrea Fuster

Eindhoven University of Technology, Eindhoven, The Netherlands
{H.J.C.E.Sengers,L.M.J.Florack,A.Fuster}@tue.nl

Abstract. Based on diffusion tensor imaging (DTI), one can construct a Riemannian manifold in which the dual metric is proportional to the DTI tensor. Geodesic tractography then amounts to solving a coupled system of nonlinear differential equations, either as initial value problem (given seed location and initial direction) or as boundary value problem (given seed and target location). We propose to furnish the tractography framework with an uncertainty quantification paradigm that captures the behaviour of geodesics under small perturbations in (both types of) boundary conditions. For any given geodesic this yields a coupled system of linear differential equations, for which we derive an exact solution. This solution can be used to construct a *geodesic tube*, a volumetric region around the fiducial geodesic that captures the behaviour of perturbed geodesics in the vicinity of the original one.

Keywords: Diffusion tensor imaging · Uncertainty quantification · Geodesic tractography · Geodesic deviation · Riemannian geometry

1 Introduction

Geodesic tractography for diffusion weighted magnetic resonance imaging (DWI) asserts that neuronal tracts are geodesics relative to some data induced metric. In the case of diffusion tensor imaging (DTI) a Riemannian metric presents itself, since its tensorial type matches that of the diffusion tensor. Indeed, from a heuristic point of view a connection between DTI and Riemannian geometry is intuitive if one stipulates the *dual* metric to be proportional to the diffusion tensor [13,15], for in that case short paths are tantamount to high diffusivity pathways, reflecting the preferred orientation of white matter tracts in line with the vestigial idea of classical streamline tractography. Finally, the Hopf-Rinow theorem [12] guarantees the existence of at least one tentative geodesic tract between any given pair of points, which may contribute to efforts of minimising false negatives. Clearly this compels us to furnish the method with an explicit criterion for pruning false positives. We will refer to the comprehensive framework accounting for all these observations as the *Riemann-DTI paradigm*[1].

---

[1] The manifest inclusion of a geodesic pruning criterion actually requires a coupling to Euclidean geometry, so a more accurate designation would be 'Riemann-Euclidean-DTI paradigm'.

The qualitative plausibility of the Riemann-DTI paradigm has been confirmed in numerous experiments on real and synthetic data. However, despite adaptations proposed to overcome shortcomings [4,8,11], state of the art geodesic tractography does not, in general, produce quantitative results. This is not surprising, since complex fiber configurations induce articulated diffusivity profiles that cannot be captured by DTI and, a fortiori, by any Riemann-DTI paradigm, due to insufficient degrees of freedom. But even in the restricted case of 'single fiber coherence', with neatly aligned axons forming smooth bundles, the stipulation of an unambiguous correspondence between DTI data and Riemannian metric consistent with white matter organisation may be too much to hope for. Water diffusion and axon geometry are, albeit correlated, entirely different things.

Nevertheless, by virtue of its non-invasive nature, intuitive appeal and relative simplicity, DTI does have clinical potential. In this article we explore avenues to make the Riemann-DTI paradigm amenable for use in the neurosurgical workflow [16]. One crucial aspect, highlighted in this endeavour, is the quantitative effect of *perturbations* of seed and target regions in tractography. In this article we adopt a generic approach, applicable to any Riemann-DTI paradigm. The precise form of the metric is immaterial for our analysis, although we will illustrate results for a particular instance.

We stress that our goal is not overly ambitious. Inevitable model errors (such as the inadequacy of DTI or of a particular Riemann-DTI paradigm) are not considered. What we aim to accomplish is to avoid conveying a false sense of faith in crisp tractography results towards the clinician, an inherent risk of any deterministic method. We do so by furnishing the Riemann-DTI paradigm with a rigorous uncertainty analysis detailed in the next section. The uncertainty alluded to is of a *fundamental* nature and cannot be removed or diminished without data-extrinsic knowledge.

2   Theory

We address the stability of geodesic tractography in the sense of robustness to generic perturbations of initial or boundary conditions. We focus on how such perturbations affect a tractogram in terms of a conservative estimate of uncertainty that prevails regardless of additional sources of uncertainty along a tractography pipeline, such as DTI data noise. This 'intrinsic' uncertainty enables a fair comparison between different tractography results, since geometrical differences can only be meaningfully quantified if one accounts for the empirical margins of uncertainty.

We depart from a metric tensor field $g_{ij}(x)$ on an n-dimension manifold $\mathcal{M}$ and a pair of unperturbed initial or boundary conditions,

$$(x(0), \dot{x}(0)) \doteq (x_0, v_0), \quad \text{or} \tag{1a}$$

$$(x(0), x(T)) \doteq (x_0, x_T), \tag{1b}$$

for a fiducial geodesic path $x = x(t)$, $t \in [0, T]$, with $\dot{x}(t) \doteq dx(t)/dt$. By virtue of the second order nature of geodesic tractography and the geodesic completeness theorem, recall Sect. 1, there are no a priori constraints on the components of each pair. We then consider two types of perturbations, representing variations of (1a) or (1b):

$$(\overline{x}_0, \overline{v}_0) = (x_0, v_0) + \eta(z_0, w_0) + \mathcal{O}(\eta^2) \,, \tag{2a}$$

$$(\overline{x}_0, \overline{x}_T) = (x_0, x_T) + \eta(z_0, z_T) + \mathcal{O}(\eta^2) \,. \tag{2b}$$

The parameter $0 \leq \eta \ll 1$ is dimensionless. Terms of order $\mathcal{O}(\eta^2)$ are considered negligible and will be suppressed henceforth.

The geodesic equation for $x = x(t)$ is given, component-wise relative to some coordinate basis, by

$$\ddot{x}^i + \Gamma^i_{jk}(x)\dot{x}^j\dot{x}^k = 0 \,, \tag{3}$$

assuming arclength parametrization relative to the metric $g_{ij}(x)$ and employing summation convention [14, 17]. The Christoffel symbols in (3) are given by

$$\Gamma^i_{jk} = \frac{1}{2}g^{i\ell} \left(\partial_j g_{\ell k} + \partial_k g_{j\ell} - \partial_\ell g_{jk} \right) . \tag{4}$$

As usual, g^{ij} indicates the components of the Gram matrix of the dual metric, i.e., $g^{ik}g_{kj} = \delta^i_j$. We furnish (3) with either (1a) or (1b), and consider a perturbed path

$$\overline{x}^i(t; \eta) = x^i(t) + \eta z^i(t) \,, \tag{5}$$

induced by (2). Each boundary condition, either (1a) or (1b), guarantees the existence of a unique solution to (3) within a sufficiently small tubular neighbourhood of the unperturbed trajectory $x(t)$. The requirement that the perturbed path (5) represents itself a geodesic for any sufficiently small η imposes constraints on the function $z = z(t)$. Technically, it is, unlike the coordinate path $x = x(t)$, *vector-valued.* From a geometric point of view this is rigorously justified if one regards (5) as the first order expansion of a parametrized geodesic congruence with parameter η (keeping t fixed), induced by the tangent vector

$$z(t) \doteq \left. \frac{\partial}{\partial \eta} \overline{x}^i(t; \eta) \right|_{\eta = 0} . \tag{6}$$

We will refer to $z(t)$ as the *deviation vector*, as it measures the first order difference between the geodesics $x(t)$ and $\overline{x}(t, \eta)$.

Inserting (5) into (3) the function $z = z(t)$ can be seen to satisfy the geodesic deviation equation [14, 17]:

$$\frac{D^2 z^i}{dt^2} + \mathrm{R}^i_{jk\ell}\dot{x}^j z^k \dot{x}^\ell = 0 \,, \tag{7}$$

in which $\mathrm{R}^i_{jk\ell}$ is the Riemann tensor :

$$\mathrm{R}^i_{jk\ell} = \partial_k \Gamma^i_{j\ell} - \partial_\ell \Gamma^i_{jk} + \Gamma^i_{km}\Gamma^m_{j\ell} - \Gamma^i_{\ell m}\Gamma^m_{jk} \,. \tag{8}$$

The operator D/dt in (7) represents a *covariant* derivative [14, 17] along $x(t)$. For the components v^i of a vector field v it is given in terms of the ordinary t-derivative and Γ-correction terms by $Dv^i/dt = dv^i/dt + \Gamma^i_{jk}v^j\dot{x}^k$.

We may rewrite (7) as a first order system:

$$
\begin{cases}
\dfrac{Dz^i}{dt} = w^i\,, \\
\dfrac{Dw^i}{dt} = -\mathrm{R}^i_{jk\ell}\dot{x}^j z^k \dot{x}^\ell\,.
\end{cases}
\tag{9}
$$

Resolving covariant derivatives in terms of ordinary derivatives and Γ-correction terms leads to

$$
\begin{cases}
\dfrac{dz^i}{dt} = w^i - \Gamma^i_{jk}z^j\dot{x}^k\,, \\
\dfrac{dw^i}{dt} = -\mathrm{R}^i_{jk\ell}\dot{x}^j z^k \dot{x}^\ell - \Gamma^i_{jk}w^j\dot{x}^k\,.
\end{cases}
\tag{10}
$$

This system can in turn be written as a homogeneous vector-valued first order ordinary differential equation of dimension $2n$:

$$
\frac{d}{dt}
\begin{bmatrix} z \\ w \end{bmatrix}
=
\begin{bmatrix} A & I_n \\ B & A \end{bmatrix}
\begin{bmatrix} z \\ w \end{bmatrix}\,,
\tag{11}
$$

in which A, B and I_n are $n\times n$-matrices with entries

$$
A^i_j \doteq -\Gamma^i_{jk}\dot{x}^k \qquad (I_n)^i_j \doteq \delta^i_j \qquad B^i_j \doteq -\mathrm{R}^i_{kj\ell}\dot{x}^k\dot{x}^\ell\,.
\tag{12}
$$

The solution may be conveniently written in terms of product integrals from multiplicative calculus, cf. Gill and Johansen [9] for a survey, and Florack and Van Assen [7] for the non-commutative case at hand. Abbreviating (11) as

$$
\frac{d}{dt}Z = MZ\,,
\tag{13}
$$

with $Z(t) = (z(t), w(t))$ and initial condition $Z_0 \doteq Z(0)$, the closed-form solution is given by

$$
Z(t) = \prod_0^t \exp\left(M(s)ds\right) Z_0\,,
\tag{14}
$$

in which exp is the matrix exponential function, and

$$
\prod_0^t \exp\left(M(s)ds\right) \doteq \lim_{N\to\infty} \exp\left(M(s^*_N)\Delta s_N\right)\ldots\exp\left(M(s^*_1)\Delta s_1\right)\,,
\tag{15}
$$

for any partitioning of the integration interval $[0, t]$, with interval widths $\Delta s_i = s_i - s_{i-1}$ and sample points $s^*_i \in [s_{i-1}, s_i]$, $i = 1, \ldots, N$, such that $s_0 = 0$, $s_N = t$. We may write (14) as $Z(t) = \Pi(t)\, Z_0$, with $2n\times 2n$ block matrix

$$\Pi(t) \doteq \prod_0^t \exp\left(M(s)ds\right) \doteq \begin{bmatrix} \Pi_{11}(t) & \Pi_{12}(t) \\ \Pi_{21}(t) & \Pi_{22}(t) \end{bmatrix}. \tag{16}$$

Using this notation, the solution $z(t)$ to the system (7) furnished with initial conditions (2a) may be succinctly expressed as

$$z(t) = \Pi_{11}(t)z_0 + \Pi_{12}(t)w_0. \tag{17}$$

If, instead of (2a), we consider endpoint perturbations of type (2b), then we must treat $w_0 \doteq w(0)$ as an unknown, such that upon setting $t = T$ in (17) we have $z(T) = z_T$. By making this substitution we obtain a relation between the unknown constant w_0 and the pair (z_0, z_T). Solving this relation for w_0 in terms of (z_0, z_T) and substituting it into (17), the solution of the boundary value problem, i.e., (7) and (2b), can be written as

$$z(t) = \left(\Pi_{11}(t) - \Pi_{12}(t)\Pi_{12}(T)^{-1}\Pi_{11}(T)\right)z_0 + \Pi_{12}(t)\Pi_{12}(T)^{-1}z_T. \tag{18}$$

Equations (17) and (18) are the closed-form solutions for our deviation vector $z(t)$ along the fiducial geodesic $x(t)$ in terms of initial, respectively endpoint perturbations, (z_0, w_0) and (z_0, z_T), recall (2). Also recall that, given $x(t)$, these closed-form expressions for $z(t)$ imply a closed-form expression for any perturbed path $\overline{x}(t)$ via (5), valid up to first order in η.

To further investigate the perturbations (2), we note that the deviation vector $z(t)$ in (5) is found to be bilinear in (z_0, w_0), respectively (z_0, z_T), recall (17) and (18). Hence we may generically write

$$z(t) = P(t)z_0 + Q(t)y. \tag{19}$$

for matrices $P(t), Q(t) \in \mathbb{R}^{n \times n}$, with either $y \doteq w_0$ or $y \doteq z_T$.

Instead of regarding the perturbation (z_0, y) as fixed, it is instructive to view it as a realization of some random variable, rendering $z(t)$ stochastic as well. In this way we are able to capture the behaviour of $z(t)$ for different perturbations (z_0, y) all at once. Let f_{z_0}, f_y be the probability density functions of the random variables z_0 and y, assuming a zero mean for both. Assuming z_0 and y to be independent of each other, the probability density $f_{z(t)}$ of $z(t)$ is given by a convolution of the densities of each of the terms in (19):

$$f_{z(t)} = \frac{1}{\det(P(t))}\frac{1}{\det(Q(t))}(f_{z_0} \circ P^{-1}(t)) * (f_y \circ Q^{-1}(t)). \tag{20}$$

This may be restated in terms of Fourier transforms[2] [10]:

$$f_{z(t)} = \mathcal{F}^{-1}\left(\left(\mathcal{F}(f_{z_0}) \circ P^{\mathrm{T}}(t)\right)\left(\mathcal{F}(f_y) \circ Q^{\mathrm{T}}(t)\right)\right), \tag{21}$$

---

[2] The Fourier transform of a probability density function, $\mathcal{F}(f)$, is also known as the *characteristic function*. It always exists and, like the density function, it completely characterizes the random variable.

in which the superscript T denotes matrix transposition. Note that (21) is valid even for singular $P(t)$ and/or $Q(t)$, unlike (20). The level sets of $f_{z(t)}$ may be used to visualize the distribution of $z(t)$ for each parameter value t. In general, however, these sets are curved surfaces embedded in $n = 3$ dimensional space and thus likely to overlap and intersect for different values of t, obfuscating the visualization. To avoid this we note that components of the deviation vectors $z(t)$ parallel to $\dot{x}(t)$ are geometrically irrelevant and may be absorbed into a reparameterization of the curve. Therefore we consider the Euclidean projection of $z(t)$ onto the plane orthogonal to the tangent vector $\dot{x}(t)$:

$$z_{\perp}(t) = \left(I_3 - \frac{\dot{x}(t)\dot{x}^{\mathrm{T}}(t)}{\|\dot{x}(t)\|^2} \right) z(t) . \tag{22}$$

The corresponding probability density $f_{z_{\perp}(t)}$ is obtained by the formal replacement in (21)

$$P(t) \mapsto P_{\perp}(t) \doteq \left(I_3 - \frac{\dot{x}(t)\dot{x}^{\mathrm{T}}(t)}{\|\dot{x}(t)\|^2} \right) P(t) , \quad Q(t) \mapsto Q_{\perp}(t) \doteq \left(I_3 - \frac{\dot{x}(t)\dot{x}^{\mathrm{T}}(t)}{\|\dot{x}(t)\|^2} \right) Q(t) , \tag{23}$$

Instead of representing tractograms as a collection of 'naked' curves, we propose the concept of *geodesic tubes*, constructed by inflating these curves to tubes with local cross sections given by the level sets of $f_{z_{\perp}(t)}$, see Fig. 1. More precisely, the tube around geodesic curve $x(t)$ is given by

$$\mathrm{Tube}(x, \beta) = \bigcup_{t \in [0,T]} \{ x(t) + \eta z : f_{z_{\perp}(t)}(z) = \beta \} , \tag{24}$$

for some parameter $\beta > 0$ controlling the extent of the level sets. By constructing geodesic tubes in this way, a non-vanishing geodesic deviation is tantamount to an inflated tube, whose volume reflects the first order geodesic path corrections induced by the stochastic perturbations at hand. Thus a geodesic tube provides an estimation of the uncertainty for any computed geodesic.

Last, we note that the visualization of geodesic tubes may be challenging in case geodesics are not sufficiently far from each other, since their tubes are likely to cause clutter. This difficulty can be overcome by constructing a probability density f from (20) or (21), by summing over x, integrating over t and suitable renormalization, so that

$$f(\xi) \propto \sum_x \int_t f_{z(t)} \left(\frac{\xi - x(t)}{\eta} \right) dt . \tag{25}$$

Recall that $f_{z(t)}$ itself, and not only through its argument, depends on x (not indicated for simplicity of notation). Equation (25) may be seen as a generalization of (20), (21) for multiple geodesics, representing the probability to find a perturbed trajectory induced by *any* of the unperturbed geodesics. The level set $\{ f(\xi) = \beta \}$ represents the uncertainty arising from a collection of geodesics due to perturbations in initial or boundary conditions, and it is the generalization of (24).

3   Experiments

We perform experiments on two clinical DWI datasets, acquired with a Philips Achieva 3T MRI scanner (b = 1500, 50 diffusion-weighting directions, six b = 0 images, 2 mm isotropic voxel size). Note that throughout our experiments the dimension of space is $n = 3$ and the defining Gram matrix for our Riemann-DTI paradigm is the adjugate of the DTI matrix D, $g_{ij} = \det D\, D_{ij}^{\text{inv}}$, cf. Fuster et al. [8] for a geometric motivation. In the experiments we restrict ourselves to perturbations of type (2b), so that $y \doteq z_T$ in (19). Perturbations of type (2a) will induce tubes with ever growing cross sections, corresponding to the accumulation of errors when solving (7) as an initial value problem; in this case we cannot expect the first order approximation (5) to hold along the entire geodesic. By restricting ourselves to perturbations of type (2b) we ensure that, at least near the two endpoints, the perturbations are sufficiently small.

We assume variables z_0, z_T to follow normal distributions $\mathcal{N}(0, I_3)$, in which case $z_\perp(t)$ is also normally distributed with covariance matrix

$$\Sigma_\perp(t) = P_\perp(t)P_\perp^{\text{T}}(t) + Q_\perp(t)Q_\perp^{\text{T}}(t)\,. \tag{26}$$

From the expression

$$f_{z_\perp(t)}(\xi) = \frac{1}{\sqrt{(2\pi)^2 \det(\Sigma_\perp(t))}} \exp\left(-\frac{1}{2}\xi^{\text{T}}\Sigma_\perp^{-1}(t)\xi\right) \tag{27}$$

it is clear that the level sets are determined by the quadratic form $\xi \mapsto \xi^{\text{T}}\Sigma_\perp^{-1}(t)\xi$ and thus will be elliptical. We set the parameters in (24) to $\eta = 1.0$ and $\beta = 0.1/\sqrt{(2\pi)^2 \det(\Sigma_\perp(t))}$. Parameter β is chosen such that the integral of $f_{z_\perp(t)}$ over the superlevel set $\{\xi : f_{z_\perp(t)}(\xi) \geq \beta\}$ is 0.9, i.e., so that the tube covers 90% of the probability distribution $f_{z_\perp(t)}$.

Figure 1 illustrates the construction of geodesic tubes for two arbitrarily chosen, unperturbed geodesics, in relation to explicitly computed neighbouring geodesics (from explicitly perturbed endpoints). The geodesic tubes enclose most of the perturbed geodesics, except for a few in the bottom right illustration. In both cases, the ellipses representing the level sets become almost degenerate indicating a unidirectional deviation, which is in agreement with the perturbed geodesics. Although we do not satisfy the 'usual' constraint for linear perturbation theory[3], viz. $\eta \ll 1$, we still obtain plausible results. In the bottom right illustration we notice perturbed geodesic curves running (partly) outside the interior of the tube, but upon closer inspection we find that these curves have boundary values z_0, z_T, fairly distant from x_0, x_T. It no surprise then, that the first order approximation underlying the geodesic tube ceases to be valid.

---

[3] The role of η is confounded with the widths of the probability distributions for z_0 and z_T by virtue of (2). If these are sufficiently narrow, then η is a formal parameter that may be set to 1 without loss of generality.
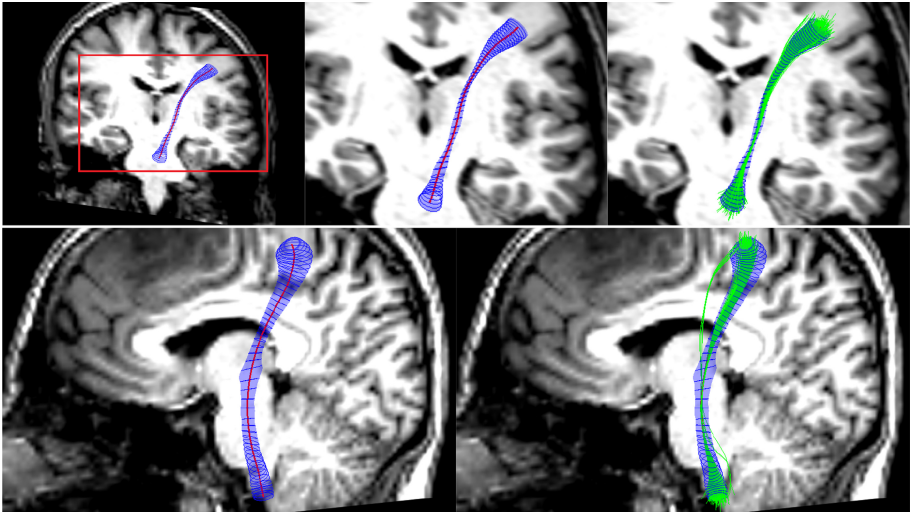
Fig. 1. Left: In red, two arbitrarily chosen geodesics between a seedpoint in the brain stem and a target in the precentral gyrus. In translucent blue, the associated geodesic tubes, cf. Eq. (24). **Right**: In green, 40 perturbed geodesics in the vicinity of the original, unperturbed geodesics. Note that the perturbed boundary values do not need to be confined to the plane perpendicular to $\dot{x}(0)$, respectively $\dot{x}(T)$. (Color figure online)

Figure 2 presents a qualitative comparison of the Cortico Spinal Tract (CST). We generated 5000 geodesics and their associated densities $f_{z(t)}$. Every unperturbed geodesic gives rise to 40 perturbed ones, yielding a total of 2×10^5 geodesics, which are explicitly computed for the sake of this experiment by repeatedly solving (3) with boundary conditions (2b). Our proposed alternative avoids solving—in principle arbitrarily many—nonlinear differential equations for neighbouring geodesics via (3), solving instead a single linear differential equation for a representative geodesic tube, recall (7). Our experiments indicate that the computation of geodesic tubes may indeed be a feasible strategy as long as the perturbations remain sufficiently small. To ensure that we only illustrate geodesics having this property, we compute from the densities in (27) the pointwise expectation value $\mathbb{E}[\|z_\perp(t)\|_2]$, and subsequently the tractwise quantity

$$M = \max_{t \in [0,T]} \mathbb{E}[\|z_\perp(t)\|_2]. \tag{28}$$

Of the 5000 computed tracts, only 2352 (resp. 2170) are used in determining the density f in (25), viz. those for which $M \leq 3\,\mathbb{E}[\|z_\perp(0)\|_2] = 3\sqrt{\pi/2} \approx 3.75$. Although in no way rigourous, this ad-hoc threshold allows us to impose the condition that deviations are sufficiently small, ensuring validity of (5). The images on the left show the 90% level set of the densities f and the ones on the right illustrate the empirical densities of the perturbed geodesics, obtained by counting how many of them pass through each voxel.

Figure 3 presents a comparison between the geodesic tubes and the iFOD2 probabilistic fiber tracking algorithm of MRtrix3 [18]. In both the geodesic and the probabilistic MRtrix3 tracking, we have constrained the tracts of the right Inferior Fronto-Occipital Fasciculus (IFOF) to pass through the capsula externa. This criterion is induced by anatomical prior knowledge and not by the usage of geodesic deviation. Results in Fig. 3 show a good qualitative agreement between probabilistic and geodesic tracking.

4   Discussion

We have addressed the stability of geodesic tractography in the sense of its robustness to perturbations of initial or boundary conditions. By perturbing such conditions for a fiducial geodesic, the first order effect on the considered geodesic is analytically computed for the first time (for a general metric), using the well-known geometric concept of geodesic deviation. Based on this, we have proposed the idea of *geodesic tubes* to visually capture the collective behaviour of perturbed tracts in the vicinity of the original geodesic.

Our experiments indicate that the computation of geodesic tubes (for a relatively sparse set of geodesics with uncertain boundary conditions) may indeed be a feasible strategy, providing both an estimation of the uncertainty for any computed geodesic as well as a dimensionality reduction principle for handling massive bundles of geodesics, as long as perturbations remain sufficiently small. Such reduction is gained by solving a single linear differential equation instead of, in principle, arbitrarily many, non-linear differential equations. This leads to a computational efficiency which favours our analytical approach over practical methods, e.g., brute force Monte Carlo simulations. At the same time the experiments reveal the need for an operational definition of what 'sufficiently small' means in this context. The appropriate length scales must somehow be induced by the local data structure, which we will address in future work.

Our framework can be extended in several ways. Firstly, instead of perturbed boundary conditions we may consider perturbations of the metric tensor field g_{ij} induced by DTI noise. This leads to an inhomogeneous geodesic deviation equation, generalizing (7), in which an additional force term is active along the entire geodesic path. This extension will be studied in future work.

Secondly, we may consider the more general Finsler-DWI paradigm [1–3,5,6], stipulated as a 'canonical' extension of the Riemann-DTI paradigm. Such a Finslerian extension offers the advantages that (i) an analogous geometric description of geodesic tractography and perturbative effects applies, albeit mathematically more cumbersome, and (ii) the descriptive power is greatly enhanced by the removal of the quadratic restriction underlying the Riemann-DTI paradigm (i.e., the limitation to DTI, respectively to inner product induced norms), making it the natural choice for an unconstrained DWI (HARDI) representation. Thus our perturbative analysis is potentially relevant beyond the scope of Riemann-DTI.
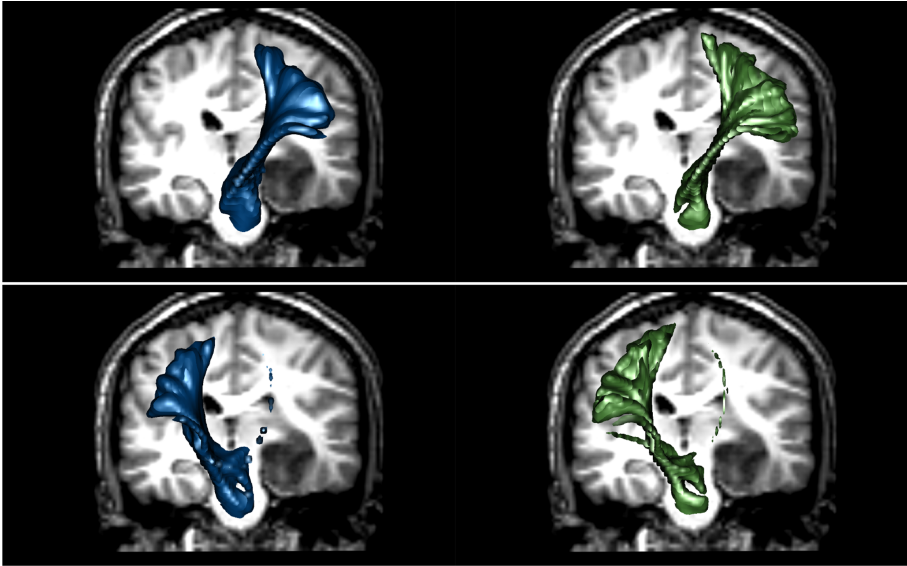
Fig. 2. Anterior view of a coronal cross section of a DWI scan with a tumor on the left side of the brain. **Left**: Density of the geodesic deviation, as per (25). Such accumulated density over all unperturbed geodesics prevents clutter arising from geodesics and corresponding tubes being too close to each other. **Right**: Empirical density of the perturbed geodesics obtained by counting how many of them pass through each voxel. Every one of the 5000 unperturbed geodesics generates 40 perturbed geodesics. In total we have solved nonlinear differential equation (3) 2×10^5 times, in contrast to the construction of the densities in (20) or (21), which requires both (3) and (7) to be solved just 5000 times, illustrating the computational profit gained from the use of geodesic tubes.

Fig. 3. Sagittal cross section of the same DWI scan as in Fig. 2. **Left**: Density induced by tracts from the right Inferior Fronto-Occipital Fasciculus (IFOF), as per (25). Of the 5000 computed tracts, only 1264 have been used in (25), viz. those which pass through the capsula externa and satisfy $M \leq 3\sqrt{\pi/2}$. **Right**: 2514 tracts generated by MRtrix3 FOD-based probabilistic fiber tracking of the right IFOF, again including only tracts that pass through the capsula externa.

References

1. Astola, L.J., Florack, L.M.J.: Finsler geometry on higher order tensor fields and applications to high angular resolution diffusion imaging. Int. J. Comput. Vision **92**(3), 325–336 (2011). https://doi.org/10.1007/s11263-010-0377-z
2. Dela Haije, T., et al.: Structural connectivity analysis using Finsler geometry. SIAM J. Imag. Sci. **12**(1), 551–575 (2019). https://doi.org/10.1137/18M1209428
3. Dela Haije, T.C.J.: Geometry in Diffusion Weighted MRI. Ph.D. thesis, Eindhoven University of Technology, Eindhoven, The Netherlands (16 May 2017)
4. Dong, X., Zhang, Z., Srivastava, A.: Bayesian tractography using geometric shape priors. Front. Neurosci. **11** (2017). https://doi.org/10.3389/fnins.2017.00483
5. Hotz, I., Schultz, T. (eds.): Visualization and Processing of Higher Order Descriptors for Multi-Valued Data. MV. Springer, Cham (2015). https://doi.org/10.1007/978-3-319-15090-1
6. Westin, C.-F., Vilanova, A., Burgeth, B. (eds.): Visualization and Processing of Tensors and Higher Order Descriptors for Multi-Valued Data. MV. Springer, Heidelberg (2014). https://doi.org/10.1007/978-3-642-54301-2
7. Florack, L., van Assen, H.: Multiplicative calculus in biomedical image analysis. J. Math. Imaging Vis. **42**(1), 64–75 (2012)
8. Fuster, A., Dela Haije, T., Tristán-Vega, A., Plantinga, B., Westin, C.-F., Florack, L.: Adjugate diffusion tensors for geodesic tractography in white matter. J. Math. Imaging Vis. **54**(1), 1–14 (2015). https://doi.org/10.1007/s10851-015-0586-8
9. Gill, R.D., Johansen, S.: A survey of product-integration with a view toward application in survival analysis. Ann. Stat. **18**, 1501–1555 (1990)
10. Grimmett, G.R., Stirzaker, D.R.: Probability and Random Processes, 4th edn. Oxford University Press (2020)
11. Hao, X., Zygmunt, K., Whitaker, R.T., Fletcher, P.T.: Improved segmentation of white matter tracts with adaptive Riemannian metrics. Med. Image Anal. **18**, 161–175 (2014). https://doi.org/10.1016/j.media.2013.10.007
12. Hopf, H., Rinow, W.: Ueber den Begriff der vollständigen differentialgeometrischen Fläche. Commentarii Mathematici Helvetici **3**(1), 209–225 (1931). https://doi.org/10.1112/blms/7.3.261
13. Lenglet, C., Deriche, R., Faugeras, O.: Inferring white matter geometry from diffusion tensor mri: application to connectivity mapping. In: Pajdla, T., Matas, J. (eds.) ECCV 2004. LNCS, vol. 3024, pp. 127–140. Springer, Heidelberg (2004). https://doi.org/10.1007/978-3-540-24673-2_11
14. Lovelock, D., Rund, H. (eds.): Tensors, Differential Forms, and Variational Principles. Dover Publications Inc., Mineola (1988)

15. O'Donnell, L., Haker, S., Westin, C.-F.: New approaches to estimation of white matter connectivity in diffusion tensor MRI: elliptic pdes and geodesics in a tensor-warped space. In: Dohi, T., Kikinis, R. (eds.) MICCAI 2002. LNCS, vol. 2488, pp. 459–466. Springer, Heidelberg (2002). https://doi.org/10.1007/3-540-45786-0_57
16. Rutten, G.J.M., Kristo, G., Pigmans, W., Peluso, J., Verheul, H.B.: Het gebruik van MR-tractografie in de dagelijkse neurochirurgische praktijk. Tijdschrift voor Neurologie Neurochirurgie **115**(4), 204–211 (2014). With English abstract
17. Tu, L.W.: Principal bundles and characteristic classes. Differential Geometry. GTM, vol. 275, pp. 241–291. Springer, Cham (2017). https://doi.org/10.1007/978-3-319-55084-8_6
18. Tournier, J.D., et al.: MRtrix3: a fast, flexible and open software framework for medical image processing and visualisation. Neuroimage **202** (2019). https://doi.org/10.1016/j.neuroimage.2019.116137